



**Potential of multispectral synergism for observing ozone pollution by combining IASI-NG and UVNS  
measurements from EPS-SG satellite**

**Lorenzo Costantino<sup>(1)</sup>, Juan Cuesta<sup>(1)</sup>, Emanuele Emili<sup>(2)</sup>, Adriana Coman<sup>(1)</sup>, Gilles Foret<sup>(1)</sup>, Gaëlle  
5 Dufour<sup>(1)</sup>, Maxim Eremenko<sup>(1)</sup>, Yohann Chailleux<sup>(1)</sup>, Matthias Beekmann<sup>(1)</sup>, Jean-Marie Flaud<sup>(1)</sup>**

<sup>(1)</sup> *LISA, CNRS UMR7583 Université Paris-Est Créteil et Université Paris Diderot  
61 Av. Général de Gaulle, 94010, Créteil, France*

10 <sup>(2)</sup> *CERFACS  
42 Av. G. Coriolis, 31057, Toulouse, France*

**ABSTRACT**

Present and future satellite observations offer a great potential for monitoring air quality on daily and global  
15 basis. However, measurements from currently in orbit satellites do not allow using a single sensor to probe  
accurately surface concentrations of gaseous pollutants such as tropospheric ozone (Liu et al., 2010). Using  
single-band approaches based on spaceborne measurements of either thermal infrared radiance (TIR,  
**Eremenko et al., 2008**) or ultraviolet reflectance (UV, **Liu et al., 2010**) only ozone down to the lower  
troposphere (3 km) may be observed. A recent multispectral method (referred to as IASI+GOME-2)  
20 combining the information of IASI and GOME-2 (both onboard MetOp satellites) spectra, respectively from  
the TIR and UV, has shown enhanced sensitivity for probing ozone at the lowermost troposphere (LMT,  
below 3 km of altitude) with maximum sensitivity down to 2.20 km a.s.l. over land, while sensitivity for  
IASI or GOME-2 only peaks at 3 to 4 km at lowest (**Cuesta et al., 2013**). Future spatial missions will be  
launched in the upcoming years, such as EPS-SG, carrying new-generation sensors of IASI and GOME-2  
25 (respectively IASI-NG and UVNS) that will enhance the capacity to observe ozone pollution and particularly  
by synergism of TIR and UV measurements.

In this work we develop a pseudo-observation simulator and evaluate the potential of future EPS-SG satellite  
observations through IASI-NG+UVNS multispectral method to observe near-surface O<sub>3</sub>. The pseudo-real  
state of atmosphere (nature run) is provided by the MOCAGE (MOdèle de Chimie Atmosphérique à Grande  
30 Échelle) chemical transport model. Simulations are calibrated by careful comparisons with real data, to  
ensure the best consistency between pseudo-reality and reality, as well as between the pseudo-observation  
simulator and existing satellite products. We perform full and accurate forward and inverse radiative transfer  
calculations for a period of 4 days (8-11 July 2010) over Europe.



In the LMT, there is a remarkable agreement in the geographical distribution of O<sub>3</sub> partial columns, calculated between the surface and 3 km of altitude, between IASI-NG+UVNS pseudo-observations and the corresponding MOCAGE pseudo-reality. With respect to synthetic IASI+GOME-2 products, IASI-NG+UVNS shows a higher correlation between pseudo-observations and pseudo-reality, enhanced by about 11%. The bias on high ozone retrieval is reduced and the average accuracy increases by 22%. The sensitivity to LMT ozone is enhanced on average with 154% (from 0.29 to 0.75, over land) and 208% (from 0.21 to 0.66, over ocean) higher degrees of freedom. The mean height of maximum sensitivity for the LMT peaks at 1.43 km over land and 2.02 km over ocean, respectively 1.03 km and 1.30 km below that of IASI+GOME-2. IASI-NG+UVNS shows also good retrieval skill in the surface-2km altitude range with a mean DOF (degree of freedom) of 0.52 (land) and 0.42 (ocean), and an average H<sub>max</sub> (altitude of maximum sensitivity) of 1.29 km (land) and 1.96 km (ocean).

Unique of its kind for retrieving ozone layers of 2-3 km thickness, in the first 2-3 km of the atmosphere, IASI-NG+UVNS is expected to largely enhance the capacity to observe ozone pollution from space.

## 1 Introduction

The retrieval of tropospheric ozone is a major issue for air quality studies. Ground-level ozone is a priority air pollutant, causing approximately 22,000 excess deaths per year in Europe (Amann et al., 2005). Current (e.g., MetOp, EOS-Aura, ADEOS) and future (e.g., EPS-SG, MTG-S) satellite observation systems offer a great potential for monitoring air quality on daily and global basis. Because of their global coverage every day, they can be used in synergy with regional Chemical Transport Models (CTM) for full data assimilation (e.g., Coman et al., 2012) or inter-validation (e.g., Zyryanov et al., 2012). Recent spaceborne instruments as the Infrared Atmospheric Sounding Interferometer IASI (Clerbaux et al., 2009) and the Global Ozone Monitoring Experiment-2 GOME-2 (EUMETSAT, 2006), onboard MetOp satellite, offer a daily global coverage appropriate for monitoring pollution. Their ground resolution is relatively fine, with four 12 km-diameter pixels spaced by 25 km (at nadir) for IASI and 80×40 km<sup>2</sup> ground pixels for GOME-2.

Both TIR and UV observations are able to provide vertical information on ozone concentration. UV sounders were traditionally used for the stratosphere but recently also for the troposphere (e.g. Liu et al., 2010) and TIR sensors are particularly sensitive to tropospheric ozone, down to the lower troposphere (below 6 km of altitude, Eremenko et al., 2008). However, it has been shown that using spaceborne observations from one spectral domain (either TIR or UV), only ozone down to 3-4 km of altitude at lowest may be observed (Foret et al., 2014). Recent studies combine the information on ozone distribution from radiance measurements of different spectral domains. Numerical studies (Landgraf and Hasekamp, 2007; Worren et al., 2007) showed a significant improvement in the sensitivity to retrieve ozone in the lowest 5 km of the troposphere combining TIR and UV measurements respectively from TES (Tropospheric Emission Spectrometer) and OMI (Ozone Monitoring Instrument) sounders (both onboard Aura satellite).

More recently, new retrieval approaches have shown the capability to derive ozone profiles from the multispectral synergism from real satellite measurements at the TIR and UV. Fu et al. (2013) combined



measurements from TES (for TIR) and OMI (for UV) sensors and founded a clear improvement in retrieval sensitivity and vertical resolution in the troposphere as well as a sensitivity and accuracy enhancement below 700 hPa, compared with either instrument alone. Cuesta et al. (2013) developed a multispectral synergism of IASI (for TIR) and GOME-2 (for UV) spectra capable of observing for the first time from space ozone  
75 plumes located below 3 km of altitude, defined here as the lowermost troposphere (LMT). The latter approach (referred to as IASI+GOME-2 and used in the following of this paper) decreases the altitude of maximum sensitivity of O<sub>3</sub> satellite retrievals, peaking on average at 2.2 km height over land (about 800 m below single-band methods), and enhances the degree of freedom in the LMT by about 40% with respect to single-band retrievals. IASI+GOME-2 uses two radiative transfer codes, KOPRA (Karlsruhe Optimized and  
80 Precise Radiative transfer Algorithm) and VLIDORT (Vector Linearised Discrete Ordinate Radiative Transfer). The inversion algorithm is integrated in the inversion module KOPRAfit. It uses a Tikhonov-Phillips-type altitude dependent regularisation that optimizes sensitivity to LMT (Eremenko et al., 2008), maximizing the degree of freedom (DOF) and minimizing the total retrieval error simultaneously.

Incoming satellite missions are expected to carry new-generation instrumentation capable to provide more  
85 accurate observations of tropospheric composition closer to the surface. This is the case of IASI-NG (Infrared Atmospheric Sounding Interferometer-New Generation) and UVNS (Ultraviolet Visible Near-infrared Shortwave-infrared) spectrometers, onboard the future satellite EPS-SG (EUMETSAT Polar System Second Generation) which is expected to be launched in 2022 on a polar-orbit, similarly to MetOp. UVNS instrument is part of the ESA mission Sentinel-5 payload, dedicated to monitoring the composition of the  
90 atmosphere for Copernicus Atmosphere Services.

The advent of these new-generation sensors may allow significant advances in LMT ozone sensing and air quality monitoring. This enhancement needs to be accurately quantified in order to prepare air quality monitoring systems for these future satellite products.

95

## 2 Purpose and strategy

The objective of this work is to provide a quantitative assessment of the potential of upcoming new-generation space-based observing systems for monitoring ozone pollution. In particular, we investigate the performance of the multispectral synergism of IASI-NG (for TIR emitted spectra) and UVNS (for UV  
100 backscattered radiances) measurements. IASI-NG will have half of IASI radiometric noise and a factor 2 finer spectral resolution (see Table 1). UVNS will have a higher signal-to-noise ratio (SNR) than GOME-2, a much finer horizontal resolution but a factor 2 coarser spectral resolution. To estimate the performances and errors associated to IASI-NG+UVNS, we adapt the existing IASI+GOME-2 retrieval approach to the technical specifications of IASI-NG and UVNS (Table 1). Hereafter, this method will be referred to as IASI-  
105 NG+UVNS.

We set up a Pseudo-Observation Simulator (POS) which is part of an Observing System Simulation Experiment (OSSE). OSSEs are specific type of sensitivity analysis used to quantify the expected added



value of an Observing System (OS). They have been largely used to analyse the gain of future satellite missions on trace gases monitoring (Edwards et al., 2009; Claeyman et al., 2011; Zoogman et al., 2011) and are generally composed of three elements: a nature run, a pseudo-observation simulator and an assimilation run. The nature run defines the pseudo-real state of the atmosphere for the experiment (Masutani et al., 2010). The pseudo-observation simulator generates the pseudo-retrievals. It calculates and inverts the spectra as it would be done by the observing system, simulating OS performances and errors. The assimilation run consists in the assimilation of pseudo-retrievals into a new model simulation, different and independent from the nature run.

In this work, we only focus on the first two steps of a typical OSSE: the nature run and the simulator of synthetic retrievals, while the assimilation run is left to a further and future research effort. Pseudo-reality is generated by the chemical transport model MOCAGE (MOdèle de Chimie Atmosphérique à Grande Échelle) that simulates physical and chemical processes of atmospheric gasses and aerosol including clouds (e.g., Josse et al. 2004, Marécal et al. 2015). Classical simulations experiments usually provide approximations of the pseudo-observations by means of a predefined parametrization of the averaging kernels (AVK) that describe the retrieval method sensitivity to true vertical profiles of atmospheric species. If this procedure allows to avoid full radiative transfer calculations and costly computational time, approximated averaging kernels with no (or limited) scene-dependence may fail to replicate the variability of the full radiative transfer calculations (Sellitto et al., 2013b); complex scene-dependent parametrizations of AVK (Worden et al., 2013) may represent a more useful cost-benefits compromise in case of multispectral/multi-instrument observing systems. In order to avoid these approximations, we perform full and accurate forward and inverse radiative transfer calculations, but for a limited 4 days time period.

We pay particular attention to set-up and run the simulation experiment with a high degree of reliability. Indeed, systematic biases in the key parameters of the model control sensitivity lead to unrealistic performances of the satellite product. This is particularly true for parameters such as cloud fraction, surface temperature and temperature profiles. The consistency of pseudo-reality and POS with respect to real data and existing sensor products is analysed and validated in terms of absolute magnitude and spatial variability of a number of atmospheric variables (ozone concentration, skin temperature, temperature profile) and diagnostic parameters (degree of freedom and altitude of maximum sensitivity of the retrieval algorithm).

In the following paragraphs, we present the methodology used to set up the simulation experiment: the nature run, the forward radiative transfer calculations and retrieval scheme of the OS simulator. Then, we carry out a statistical analysis of MOCAGE pseudo-reality with respect to real IASI-GOME-2 measurements and quantify retrieval errors and sensitivity for IASI+GOME-2 and IASI-NG+UVNS. Finally, we compare pseudo-observations of 0-3 km ozone partial columns of the two observing systems.

### 3 Nature run and pseudo-observation simulator



The pseudo-reality is defined by the MOCAGE model (run at CERFACS laboratory), that provides vertical  
145 profiles of atmospheric state and composition variables on hourly basis. It uses 47 sigma-pressure hybrid  
levels up to 5 hPa (approximately 35 km of altitude) with a vertical resolution that increases from 150 m  
(lower troposphere) to approximately 1 km (stratosphere) and a horizontal resolution of  $0.2 \times 0.2$  degrees. The  
same model configuration that provides operational air quality forecasts over Europe (**Marécal et al., 2015**)  
has been used for this study. We simulate LMT ozone pollution events over Europe, from 8 to 11 July 2010.  
150 Real ozone data, from surface network stations (AIRBASE), the Laboratoire d'Aérologie (LA) IASI product  
(**Barret et al. 2011, Dufour et al., 2005**) and MLS (Microwave Limb Sounder) V4.2 retrievals have been  
assimilated into MOCAGE simulation to improve the accuracy of the modeled ozone fields at the surface, in  
the free troposphere and in the stratosphere. The assimilation is performed hourly using a 3D-Var algorithm,  
described in Jamouillé et al. (2012).

155 To simulate the multispectral retrievals from IASI+GOME-2, we select the two model grid points that are  
closest to IASI and GOME-2 ground pixels respectively. For each point, KOPRA (for TIR) and VLIDORT  
(for UV) radiative transfer codes calculate the spectra, as observed by the satellite sensors, issued from  
radiation emitted, scattered (only UV) and absorbed by the surface and the atmosphere between 0 and 60 km  
of altitude. For all profiles, the radiative transfer models have a vertical resolution of 1 km. As the MOCAGE  
160 model top is set at 35 km of altitude, we complete the atmospheric vertical information between 30 and 50  
km with data from a global MOCAGE simulation, run at coarser resolution and with model top at 0.1 hPa  
(**Emili et al., 2014**), and with climatological profiles above 50 km.

Radiometric random noise for IASI and GOME-2 is added to the raw spectra before their ingestion into the  
retrieval algorithm. For TIR, the nominal noise standard deviation is taken from literature as 20 nW/  
165  $(\text{cm}^2\text{cm}^{-1}\text{sr})$  (**Eremenko et al., 2008**). Therefore, we added a noise of 13 nW/ $(\text{cm}^2\text{cm}^{-1}\text{sr})$  roughly  
accounting the reduction of noise due to apodization. For UV, noise is estimated for each wavelength using  
Muller matrix radiance response elements (**Nowland et al., 2011; Cai et al., 2012**). The signal-to-noise ratio  
for GOME-2 is equal to 32, for wavelengths between 290 and 306 nm, and equal to 350 between 325 and  
340 nm. Spectra are then ingested into the IASI+GOME-2 retrieval algorithm, that assumes no error in co-  
170 localization of TIR and UV measurements: each IASI spectrum (12 km-diameter pixel) is matched with the  
co-located GOME-2 spectrum ( $80 \times 40 \text{ km}^2$ ) within a distance of 1 degree, without any averaging.  
IASI+GOME-2 retrievals are calculated at the IASI ground resolution and processed independently for each  
IASI pixel.

Partial cloud cover and aerosols are not explicitly modelled in KOPRA, but their effects in the IASI spectra  
175 are partially compensated by offsets for each TIR micro-window (**Eremenko et al., 2008; Dufour et al.,**  
**2010**). In the UV spectra calculations, pixels with partial cloud cover are treated as a mixture of clear sky and  
cloudy scenes according to the independent pixel approximation (e.g., **Cai et al., 2012**). For more details on  
IASI+GOME-2 multispectral method refer to **Cuesta et al. (2013)**

The IASI-NG+UVNS retrieval method uses the same procedure as IASI+GOME-2, accounting for some  
180 differences in the specifications of the new instruments with respect to the existing ones that are summarized



in Table 1 (for more information, visit <https://directory.eoportal.org/web/eoportal/satellite-missions>). Note that for UVNS, only the LEO-UV-2 spectral channel is considered as the pixel resolution of the LEO-UV-1 is much coarser.

UVNS will have a higher SNR than GOME-2 but only the half of its spectral resolution. IASI-NG noise and spectral resolution will be approximately the half and a factor 2 finer than those of IASI, respectively. While IASI-NG will have the same spatial resolution as IASI and hence the same footprint (as MetOp and EPS-SG will fly on a similar polar-orbit), UVNS will have a spatial resolution of 7.5 km which is much higher than that of GOME-2. To simulate IASI-NG+UVNS retrievals, we use the closest UVNS measurements with respect to IASING pixel centre.

190 For better exploiting IASI-NG+UVNS, we have designed a constrain matrix accounting for the capability of the new sensors. As done by Cuesta et al. (2013), we have adjusted the constraints to keep similar errors to IASI+GOME-2 and enhanced sensitivity between the surface and 3 km.

	IASI (MetOp-B)	IASI-NG (EPS-SG)	GOME-2 (MetOp-B)	UVNS (EPS-SG) LEO-UV-2 channel
Radiometric noise	20 nW/(cm <sup>2</sup> cm <sup>-1</sup> sr)	10 nW/(cm <sup>2</sup> cm <sup>-1</sup> sr)	-	-
Spectral resolution	0.50 cm <sup>-1</sup>	0.25 cm <sup>-1</sup>	0.22-0.28 nm (λ=290-306 nm) 0.24-0.30 nm (λ=325-340 nm)	0.5 nm (λ=300-370 nm)
SNR	-	-	32 (λ=290-306 nm) 350 (λ=325-340 nm)	1000 (λ=300-370 nm)
Spatial resolution	12 km-diameter pixel spaced by 25 km at nadir	12 km-diameter pixel spaced by 25 km at nadir	80×40 km <sup>2</sup>	7.5×7.5 km <sup>2</sup>
Spectral sampling	0.25 cm <sup>-1</sup>	0.125 cm <sup>-1</sup>	0.12 nm	0.15 nm

195

Table 1. Differences in nominal specifications of IASI-NG and UVNS (EPS-SG) with respect to IASI and GOME-2 (MetOp-B). For UVNS, only the LEO-UV-2 spectral channel is considered.

#### 200 4 Inversion algorithm and ozone retrieval

As previously mentioned, the inversion algorithm of IASI+GOME-2 is an altitude dependent Tikhonov-Phillips regularization method for satellite nadir measurements (Cuesta et al., 2013). It is integrated in the KOPRAfit module and optimized for lowermost tropospheric ozone observations. The constrain matrix and parameters are optimized to maximize the degrees of freedom and minimize the error in the LMT, retaining a sufficient accuracy in the upper troposphere and in the stratosphere (Cuesta et al., 2013). Three different

205



ozone a priori profiles, derived from climatological values of **McPeter et al. (2007)**, are selected depending on the pseudo-real tropopause height (TH). We use a mid-latitude a priori (30°-60° N) for TH between 10 and 14 km, a tropical a priori (20°-30° N) for higher TH and a polar (60°-90° N) for TH lower than 10 km. We provide here a quantitative tool to analyse and quantify the error budget associated to each algorithm. If

210 the inversion occurs in an incrementally linear regime, we can consider that the *total error* of a constrained least square fit method is separated into three components (**Rodgers, 2000**): 1) a *measurement error*, which is random and due to instrumental limitations; 2) a *smoothing error*, which is due the specific retrieval techniques and to the limited sensitivity of the radiance measurements to the vertical distribution of the considered gas; 3) a *systematic error*.

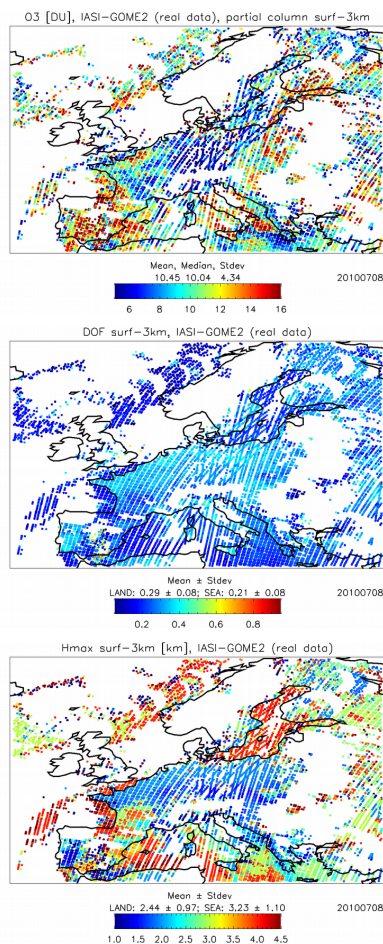
215 The KOPRAfit module provides the averaging kernel (AVK) matrix of the inversion, describing the vertical sensitivity of retrievals to true profiles. At given altitude (defined by the matrix column), each row shows the fractional height-resolved part of information for the retrieval that comes from the observed spectrum, while the remaining fraction comes from the a priori. The peak value of each AVK column indicates the height of maximum sensitivity to true profiles for the selected altitude. If we integrate the AVK over the rows (i.e.,

220 over the different altitudes), we can deduce the height of maximum sensitivity (Hmax) of the retrieval. In the following, we will be interested in the altitude of maximum sensitivity of LMT ozone retrievals, between the surface and 3 km of altitude (Hmax-3km). According to **Rodgers (2000)**, the trace of AVK matrix gives the DOF, a scalar quantity indicating the number of independent pieces of informations within a measurement. For the LMT, the DOF of ozone partial columns is obtained from the trace of AKV up to 3 km (DOF-3km).

225 It is an easy and direct parameter to quantify the vertical sensitivity of each retrieval. An example of real IASI+GOME-2 retrievals is provided in Figure 1, that shows O3 partial columns (top image) integrated between the surface and 3 km a.s.l. (O3-3km), DOF-3km (middle) and Hmax-3km (bottom) for the 08 July 2010. White gaps indicate a lack of values due to the presence of relatively high cloud cover (>30%), not available satellite data or due invalid retrievals. The DOF-3km map indicates that

230 O3-3km estimates are closer to true profiles over land, where DOF-3km is higher (0.28) than over ocean (0.22), because of a stronger thermal contrast (i.e., the temperature difference between the surface and the lowest atmospheric layer). DOF and Hmax are the two diagnostic parameters that will be used in this work to quantify the sensitivity of a retrieval method.

235



240 Figure 1. Real IASI+GOME-2 retrievals for the 08 July, 2010. Maps of O3-3km [DU] (top image), DOF-  
3km (middle), Hmax-3km [km] (bottom). White areas indicate a lack of measurements due to a cloud  
fractions higher than 0.3 or to invalid retrievals.

245 The convolution of the pseudo-reality with the AVK matrix (generally referred to as AVK-smoothing) gives  
an estimate of what retrievals would be without accounting for instrumental limitations (radiometric noise).  
The *smoothing error* is directly linked to the difference between AVK-smoothed pseudo-reality and pseudo-  
reality. It can be estimated from the standard deviation of the frequency distribution of this difference. The  
*measurement error* (i.e. due to radiometric noise) can be estimated from the standard deviation of the  
250 difference between pseudo-observations and AVK-smoothed pseudo-reality.





Finally, the difference between pseudo-observations and pseudo-reality (bias) gives an estimates of the inversion algorithm accuracy. Its standard deviation ( $\sigma$ -bias) quantifies the *total error* which is an estimate of the algorithm precision.

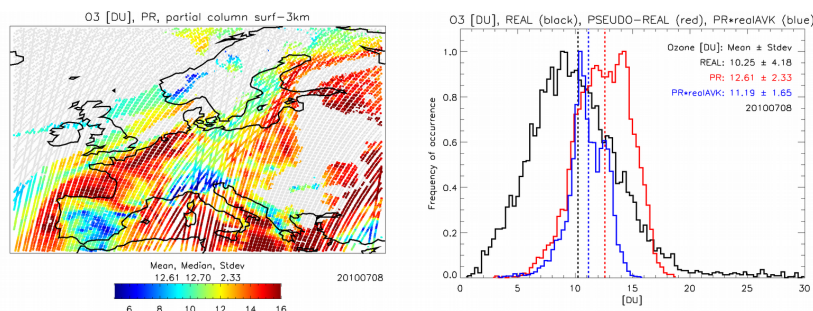
255

### 5 MOCAGE pseudo-reality

In a first analysis, we observed that MOCAGE strongly underestimates the cloud fraction (CLF), that never exceeds a value of 0.3. Therefore, we have estimated an empirical conversion from MOCAGE cloud fraction to more realistic values used as inputs of the pseudo-reality. We then compared the MOCAGE cloud fraction  
260 with GOME-2 apriori values, given from an external algorithm called FRESKO (Koelemeijer et al., 2001), for the whole 8-10 July time period. For those pixels whit  $CLF < 0.3$ , we defined two correction factors that minimize the CLF frequency distribution and the mean CLF values, between the two datasets. As the IASI+GOME-2 retrieval algorithm is not sensitive to ozone presence when  $CLF > 0.3$ , such cloudy pixels are excluded. The corrected cloud fraction results is calculated as  $CLF = 20.70 \times (CLF_{mocage}^{1.2})$ , where  
265  $CLF_{mocage}$  represents the original CLF given by MOCAGE. We assume the presence of only low clouds with cloud top pressures above 700 hPa.

As previously mentioned, a more realistic representation of ozone horizontal variability is obtained by assimilation of real ozone data into MOCAGE. To test the reliability of pseudo-real ozone concentration, we compared O3-3km from MOCAGE with real IASI+GOME-2 retrievals. Figure 2 (left) shows the map of  
270 model O3-3km data for the 08 July 2010. Light-grey indicates where cloud fraction is larger than 0.3. For consistency with Figure 1, we only show those MOCAGE pixels that would have been selected by IASI+GOME-2 algorithm on that day (i.e., co-located and near-simultaneousness with IASI and GOME-2 footprint at the time of MetOp overpass).

The normalized frequency distributions of Figure 2 (right) show an overall consistence between MOCAGE  
275 outputs and IASI+GOME-2 retrievals, in terms of O3-3km magnitude and spatial distribution. MOCAGE (red line) seems to overestimate the regional mean O3-3km by 2.16 DU (21%). This difference is mostly due to the reduced sensitivity of IASI+GOME2 retrievals to ozone below 3km of altitude. If we account for this effect, smoothing the PR by real AVK ( $PR \cdot realAVK$ ), the resulting O3-3km distribution (blue line) shows an average value much closer to real data. The positive difference of 0.74 DU (7%) that remains between  
280  $PR \cdot realAVK$  and real IASI+GOME-2 might be linked to systematic explained underestimation of cloud fraction. overestimation of ozone production in MOCAGE model, coming from the systematic underestimation of cloud fraction. A positive bias of MOCAGE at the LMT is also shown by Zyryanov et al. (2012). The larger standard deviation of IASI+GOME-2 and the smaller variability of MOCAGE outputs might be due to the radiometric noise of satellite real data and to the naturally higher variability of real data  
285 than for model simulations.

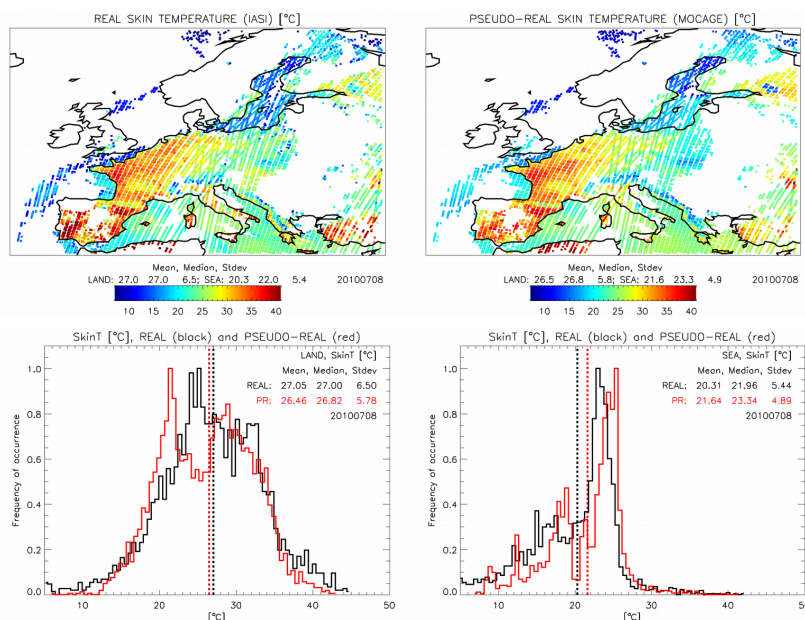


290 Figure 2. MOCAGE simulation for the 08 July, 2010. (left image) Map of pseudo-real O3-3km [DU]. For consistency with Figure 1, we consider only those MOCAGE pixels that would have been selected by IASI+GOME-2 retrieval algorithm on that day. (right image) O3-3km [DU] normalized frequency distributions of real IASI+GOME-2 measurements (black), pseudo-real MOCAGE data (red) and PR smoothed by real AVK. Dashed lines show mean O3-3km [DU] values of each distribution.

295

The analysis of pseudo-reality was also performed by comparison of surface temperatures ( $T_s$ ) from MOCAGE and retrievals, using IASI real spectra within the IASI+GOME-2 algorithm. Figure 3 shows maps of  $T_s$  derived from real IASI measurements (top left) and model simulations (top right) for the 08 July 2010, together with the histogram of their normalized frequency distribution over land (bottom left) and over ocean (bottom right). We consider only those pixels with skin temperature in the 5-45 °C range and where the absolute  $T_s$  difference between real measurements and MOCAGE is lower than 10 °C. Histograms of Figure 3 clearly indicates that MOCAGE (red) overestimates on average the ocean surface temperature and underestimates land surface temperature with respect to IASI data (black). This is true for the whole 08-10 July time period and the mean difference between real and MOCAGE  $T_s$  is equal to -1.42 °C (ocean) and +0.67 °C (land). Further analysis also shows that MOCAGE overestimates the atmospheric temperature profile in the first 6 km of altitude. For the whole period, the mean difference between real and MOCAGE temperature is equal to -2.69 (0-1km), -1.41 (1-2km), -1.51 (2-3km), -1.14 (3-4km), -0.88 (4-5km) and -0.51 (5-6km) °C. These values have been used to modify MOCAGE temperatures before running radiative calculations and inversion algorithms, in order to consider realistic thermal contrasts for pseudo-reality. It should be mentioned that this work of nature run calibration against real observations and especially for meteorological variables (important for the retrievals) is mandatory to get a realistic pseudo-reality. We believe that it is one important strength of this work to have taken care of these aspects that are often not really tackle in OSSE studies.

315



320 Figure 3. (top) maps of  $T_s$ , from real IASI measurements (left) and MOCAGE simulation (right) before  
 325 correction, for the 08 July 2010. For consistency with IASI data, we consider only those MOCAGE pixels  
 that would have been selected by IASI+GOME-2 retrieval algorithm on that day. (bottom) histograms of  $T_s$   
 normalized frequency distributions for real data (IASI, black line) and pseudo-real outputs (MOCAGE, red  
 line), over land (left) and ocean (right). Dashed lines indicate the mean value. We consider only those pixels  
 335 with skin temperature in the 5-45 °C range and where the absolute  $T_s$  difference between real measurements  
 and MOCAGE is lower than 10 °C.

## 6 Results

330 After the correction of MOCAGE cloud fraction and temperature fields toward more realistic values, we  
 have used MOCAGE atmospheric profiles to simulated TIR radiances and UV reflectances by KOPRA and  
 VLIDORT respectively. We then added radiometric random noise to raw spectra and then processed the  
 simulated spectra by IASI+GOME-2 and IASI-NG+UVNS inversion algorithms. Retrievals are provided at  
 the IASI ground resolution. Statistics of retrieval sensitivity and LMT ozone partial columns are presented in  
 335 the following paragraph.

### 6.1 Retrieval sensitivity



As previously mentioned, multispectral retrieval sensitivity is quantified in terms of lowermost tropospheric  
340 DOF and Hmax. The first row of Figure 4 shows DOF-3km maps from IASI+GOME-2 (left) and IASI-  
NG+UVNS (right). To test the general consistency of retrieval performances between the POS and reality,  
pseudo-real DOF-3km and Hmax-3km from IASI+GOME-2 (Figure 4) are compared with real satellite  
products (Figure 1). We already observed that the MOCAGE geographical distribution of O3-3km is realistic  
over Europe (Figure 1 and Figure 2). Figure 4 also shows that pseudo-real and real retrievals from  
345 IASI+GOME-2 are consistent in terms DOF-3km (first row) and Hmax-3km (second row) for both  
magnitude and spatial variability. On average, the regional DOF-3km is equal to  $0.29 \pm 0.07$  (over land) and  
 $0.21 \pm 0.05$  (over ocean) for the synthetic retrievals and to  $0.29 \pm 0.08$  (over land) and  $0.21 \pm 0.08$  (over ocean)  
for the real case. The peak of maximum sensitivity in the LMT is equal to  $2.49 \pm 0.62$  km (over land) and  
 $3.40 \pm 0.68$  (over ocean) for the synthetic retrievals and to  $2.44 \pm 0.97$  km (over land) and  $3.23 \pm 1.10$  km (over  
350 ocean) for the real case. Results are consistent (within statistical uncertainties) with real IASI+GOME-2  
sensitivity values obtained by Cuesta et al. (2013) over the same region for the 19-20 August 2009. They find  
a DOF-3km of  $0.34 \pm 0.04$  (land) and  $0.23 \pm 0.04$  (ocean), and a Hmax-3km of  $2.20 \pm 0.50$  (land) and  $3.42 \pm 0.59$   
(ocean).

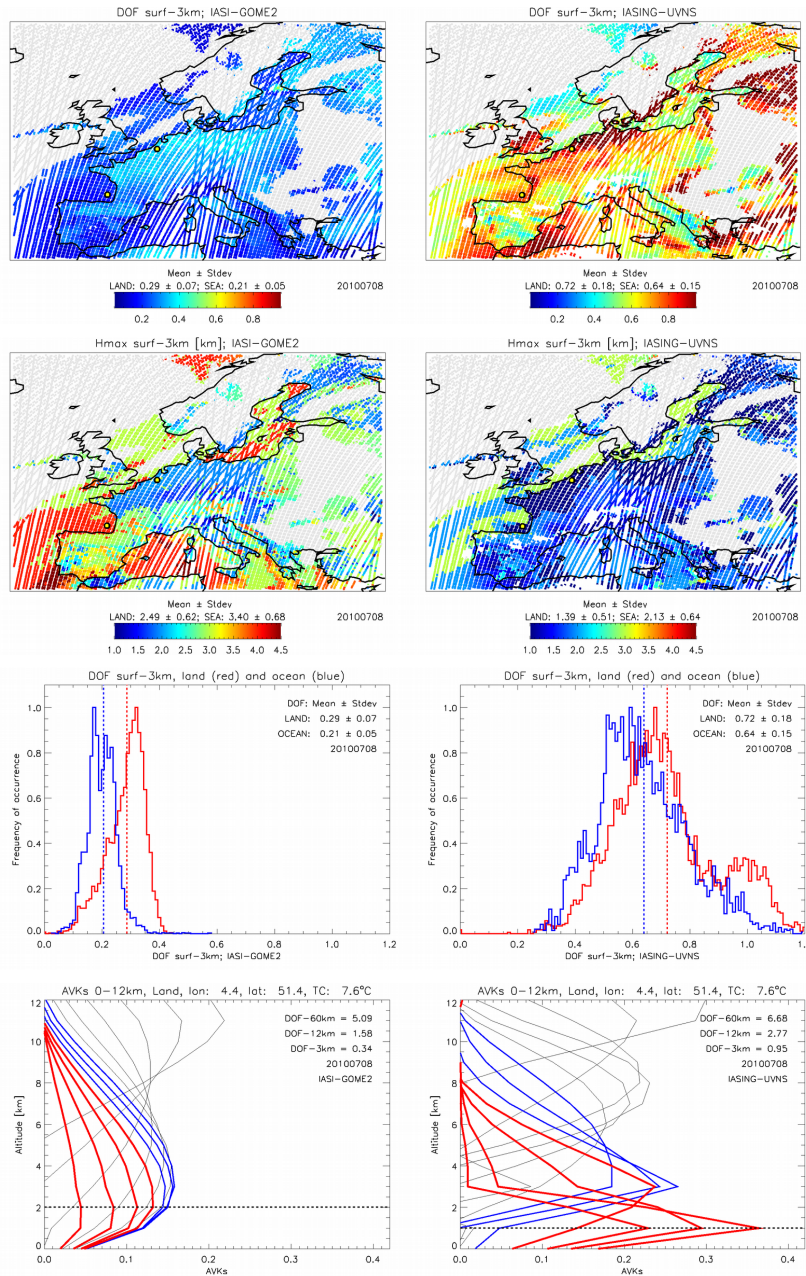
The IASI-NG+UVNS map of DOF-3km (right) shows an average increase in the degree of freedom at 3km  
355 over both land and ocean of about 150% and 200%, respectively with respect to IASI+GOME-2, with mean  
values that grow from 0.29 (land) and 0.21 (ocean) with IASI+GOME-2 to 0.72 (land) and 0.64 (ocean) with  
IASI-NG+UVNS. Note that IASI-NG+UVNS uses an optimised constraint to enhance sensitivity in the  
LMT. Accordingly, with the new spectral method the peak of LMT sensitivity to ozone (Hmax-3km, second  
row of Figure 4) decreases on average by about 1.1 km over land (from 2.50 to 1.41 km) and 1.27 km over  
360 ocean (from 3.40 to 2.13 km). Sensitivity differences between land and ocean are strong for IASI+GOME-2  
and are also present in IASI-NG+UVNS retrievals, because of the different thermal contrast which is greater  
over land. The third row of Figure 4 shows that normalized frequency distributions of DOF-3km are wider  
and shifted to higher values when using new-generation sensors (right image), with a similar mean gap of 0.8  
as for IASI+GOME-2 between land (red line) and ocean (blue line). It is remarkable that in several cases  
365 IASI-NG+UVNS method shows a DOF-3km  $\geq 0.8$  (22% of total) and a Hmax-3km  $\leq 1.5$  km (37% of  
total).

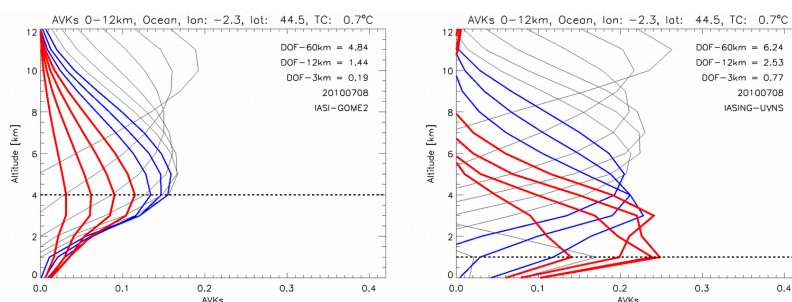
The fourth and fifth rows of Figure 4 report two examples of AVK vertical profiles at retrieval altitudes of 0,  
1, 2, 3 km (red lines) and 4, 5, 6 km (blue lines) and 7, 8, 9, 10, 11, 12 km (black lines) for two specific  
pixels over land and ocean (black-yellow spot in maps) with thermal contrast (reported in figure) particularly  
370 high and equal to  $14.5^\circ\text{C}$  (land) and  $5.9^\circ\text{C}$  (ocean). Stratospheric DOF (surface-60 km) is consistently  
increased with IASI-NG+UVNS, by 1.59 (+31%) over land and 1.40 (+29%) over ocean, and tropospheric  
DOF (surface-12km) is increased by 1.19 (+75%) over land and 1.09 (+76%) over ocean. However, the  
maximum gain is obtained in the LMT where DOF-3km increases by 0.61 (+179%) over land and 0.58  
(+305%) over ocean. The dotted line indicates the height of maximum sensitivity in the LMT. As expected,  
375 IASI+GOME-2 shows better retrieval performances over land (Hmax-3km = 2 km) than over ocean (Hmax-



3km = 4 km). The use of IASI-NG+UVNS further decreases Hmax-3km over land and even more over ocean, down to 1 km of altitude in both cases.

380





385

Figure 4. IASI+GOME-2 (left column) and IASI-NG+UVNS (right column) data, for the 08 July 2010. (first row) maps of DOF-3km pseudo-observations (PO), grey colour indicates where CLF is larger than 0.3. (second row) maps of Hmax-3km from PO. (third row) histograms of DOF-3km normalized frequency distribution from PO, over land (red) and ocean (blue). (fourth row) AKV vertical profiles at retrieval altitudes of 0, 1, 2, 3 km (red lines) and 4, 5, 6 km (blue lines) and 7, 8, 9, 10, 11, 12 km (black lines) for a pixel over land (black-yellow spot in the map) in a highly polluted area. Values of stratospheric DOF (0-60 km, referred to as “total”) and DOF-3km are reported in figure. Dashed line indicates the altitude of maximum sensitivity, in the LMT. (fifth row) same as before, but over ocean.

For the whole time period (8-11 July), averaged values of regional mean DOF-3km and Hmax-3km for IASI+GOME-2 and IASI-NG+UVNS are presented in Table 2, with real IASI+GOME-2 data reported in parenthesis next to pseudo-real ones. The IASI-NG+UVNS retrieval algorithm parametrization has been optimized to increase at most the sensitivity in the lowest layers of the atmosphere (as close as possible to human biosphere), rather than decreasing the total retrieval error. Hence, the major gain of using the multispectral synergism of EPS-SG sensors concerns DOF-3km and Hmax-3km. DOF-3km is more than doubled and tripled over land and ocean, while Hmax-3km decreases by 1.03 km and 1.3 km respectively.

400

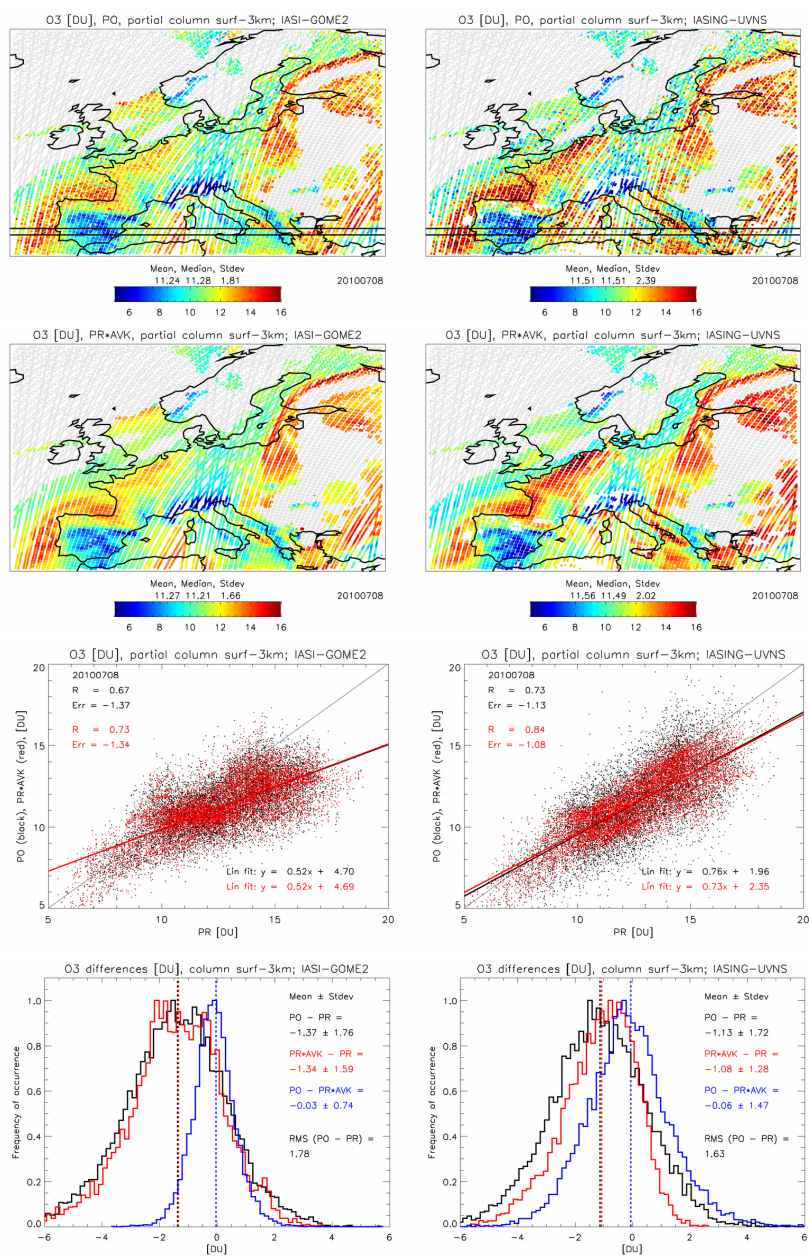
## 6.2 LMT ozone retrievals

Figure 5 shows maps of O3-3km pseudo-observations (first row) and AVK-smoothed pseudo-reality (second row), for IASI+GOME-2 (left) and IASI-NG+UVNS (right). In terms of absolute ozone concentrations, both IASI+GOME-2 and IASI-NG+UVNS have an overall good agreement with the MOCAGE pseudo-reality. The two multispectral methods differ by less than 3% in estimating the mean O3-3km value over the whole region. However IASI-NG+UVNS shows a larger spatial variability and capture more efficiently some high O3-3km values off the coast of Northern Spain, France, Holland, and Mediterranean Basin. This is even more visible looking at the AVK-smoothed pseudo-reality (Figure 5, second row), where radiometric noise is not present. O3-3km patterns smoothed by IASI-NG+UVNS averaging kernels are closer to MOCAGE product (Figure 2) because of the stronger sensitivity to true profiles.

410



415



420 Figure 5. IASI+GOME-2 (left column) and IASI-NG+UVNS (right column) data, for the 08 July 2010. (first row) maps of O3-3km pseudo-observations (PO), grey colour indicates where CLF is larger than 0.3. Black lines indicate the [38N, 39N] latitude band. (second row) maps of O3-3km from AVK-smoothed pseudo-reality (PR\*AVK). (third row) scatterplot of O3-3km [DU] from pseudo-observations (black, y-axis) and



AVK-smoothed pseudo-reality (red, y-axis) versus pseudo-reality (PR, x-axis). Linear correlation coefficient,  
 425 mean error and linear fit equation are reported in figure. (fourth row) histograms of normalized frequency  
 distribution of O3-3km differences [DU] between PO and PR (black), PR\*AVK and PR (red), PO and  
 PR\*AVK (blue). Mean value and standard deviation of each difference is reported in figure, together with  
 PO-PR root mean square (RMS).

430

As a consequence, the correlation between pseudo-retrievals and pseudo-reality is enhanced for IASI-  
 NG+UVNS. Figure 5 (third row) presents the scatterplot of O3-3km pseudo-observations (black) and AVK-  
 smoothed pseudo-reality (red), plotted in function of pseudo-reality. With respect to existing instruments (left  
 image), the product of new-generation sensors (right image) are better correlated to MOCAGE data. The  
 435 correlation coefficient increases from 0.67 to 0.73 (+9%) and the linear fit slope (reported in figure) of the  
 dispersion plot increases from 0.52 to 0.76 (+46%), sign that high O3-3km values (larger than ~8.5 DU) are  
 less underestimated.

The fourth row of Figure 5 shows the normalized frequency distributions of (pixel-by-pixel) difference in  
 O3-3km between: pseudo-observations and pseudo-reality (PO-PR, black), AVK-smoothed pseudo-reality  
 440 and pseudo-reality (PR\*AVK-PR, red), pseudo-observation and AVK-smoothed pseudo-reality (PO-  
 PR\*AVK, blue). With respect to IASI+GOME-2, the IASI-NG+UVNS mean value of PO-PR distribution  
 (retrieval mean bias) decreases from -1.37 to -1.13 (-17%) and the root mean square (RMS) from 1.78 to  
 1.63 (-8%). The standard deviation of the bias slightly decreases from 1.76 to 1.72 (-2%). Results indicate a  
 clear and global gain in retrieval accuracy (from bias and RMS) when using EPS-SG sensor instead of  
 445 MetOp instrumentation, while retrieval precision (from  $\sigma$ -bias) is not sensibly improved. This is consistent  
 with the design of the constrain matrix of IASI-NG+UVNS. For the whole time period (8-11 July), Table 2  
 reports regional means of the linear correlation coefficient R, between pseudo-observations and pseudo-real  
 data of O3-3km, as well as the bias, the  $\sigma$ -bias and the RMS of the PO-PR distribution, for both  
 IASI+GOME-2 and IASI-NG+UVNS.

450

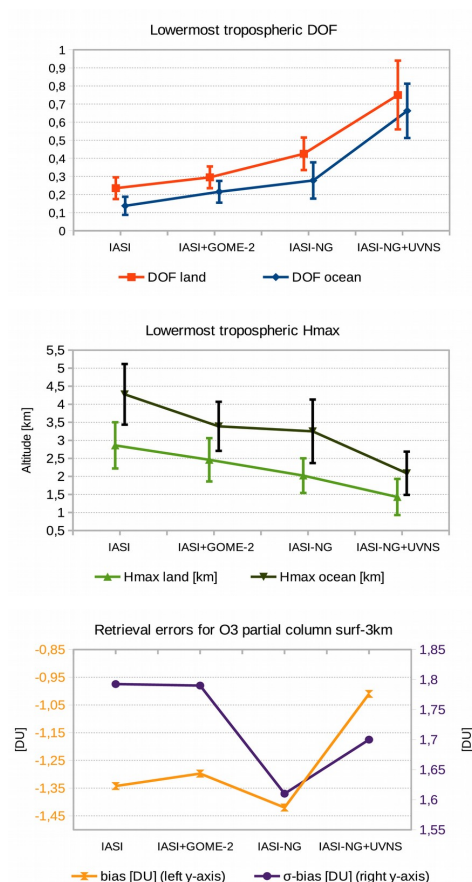
	DOF-3km		Hmax-3km [km]		R	Bias [DU]	$\sigma$ -bias [DU]	RMS [DU]
	land	ocean	land	ocean				
IASI+GOME-2	0.29±0.06	0.21±0.06	2.46±0.60	3.39±0.68	0.65	-1.30	1.79	1.77
(real)	(0.29±0.08)	(0.21±0.08)	(2.51±0.88)	(3.32±1.07)				
IASI-NG+UVNS	0.75±0.19	0.66±0.15	1.43±0.50	2.09±0.60	0.73	-1.01	1.70	1.55
Gain	+154%	+208%	-1.03	-1.30	+11%	-22%	-5%	-0.14%

Table 2. Averaged values (8-11 July 2010) of regional mean DOF-3km, Hmax-3km [km], R, bias [DU],  $\sigma$ -  
 bias [DU] and RMS [DU] of the O3-3km PO-PR distribution over Europe, for IASI-GOME-2 and IASI-





455 NG+UVNS. Real IASI+GOME-2 values of DOF-3km and Hmax-3km are reported in parenthesis next to  
 pseudo-real ones.



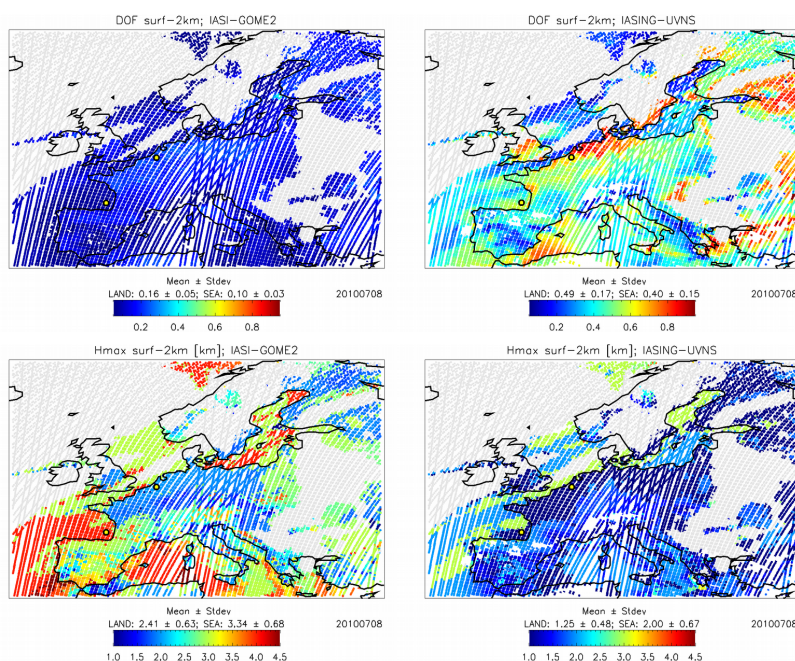
460

465 Figure 6. Average values of DOF-3km (top), Hmax-3km (middle), bias and  $\sigma$ -bias (bottom) of the O3-3km  
 PO-PR distribution over Europe for IASI, IASI+GOME-2, IASI-NG and IASI-NG +UVNS, for the whole 8-  
 11 July time period over Europe.

470 Figure 6 shows graphically the mean values of DOF-3km (middle), Hmax-3km (middle), bias and  $\sigma$ -bias  
 (bottom) of the O3-3km PO-PR distribution for IASI+GOME-2 and IASI-NG+UVNS (Table 2) together  
 with these same values for IASI and IASI-NG alone, simulated over the same area and time period. Note in  
 case of IASI alone, the POS seems to overestimate the retrieval performances with a Hmax-3km over land  
 equal to  $2.86 \pm 0.64$  km, which is only 400 m above that of IASI+GOME-2 instead of the 800 m expected by



Cuesta et al. (2013). It is evident, however, that IASI+GOME-2 represents a clear improvement to IASI  
 alone in terms of DOF-3km, Hmax-3km and bias. At the same time, the technical advances of IASI-NG  
 475 allow retrieval performances even higher than IASI+GOME-2 for what concerns DOF-3km, Hmax-3km and  
 $\sigma$ -bias. On the other hand, when IASI-NG is coupled with UVNS, the IASI-NG+UVNS synergism  
 overpasses by far the retrieval skills of all other configurations in terms of DOF-3km, Hmax-3km and bias.  
 The high quality retrieval skills of IASI-NG+UVNS in the LMT suggest to go deeper in the lowermost  
 troposphere and investigate ozone sensitivity in the surface-2km layer. Figure 7 shows the DOF-2km (top)  
 480 and the Hmax-2km (bottom) for the 8 July 2010, for IASI+GOME-2 (left) and IASI-NG+UVNS (right).  
 With respect to LMT, the retrieval performances of IASI+GOME-2 degradate sensibly in terms of DOF  
 ( $0.16 \pm 0.05$  over land  $0.10 \pm 0.03$  over ocean), as the Hmax-2km ( $2.41 \pm 0.63$  km over land and  $3.34 \pm 0.68$   
 km over ocean) remains above 2 km of latitude. On the contrary, IASI-NG+UVNS shows still a relatively high  
 DOF-2km of  $0.49 \pm 0.17$  (land) and  $0.40 \pm 0.15$  (ocean) and a Hmax-2km of  $1.25 \pm 0.48$  km (land) and  $2.0 \pm 0.67$   
 485 km (ocean), even better than IASI+GOME2 for the surface-3km partial column.  
 Averaged over the whole time period, the IASI-NG+UVNS regional mean DOF-2km is equal to  $0.52 \pm 0.17$   
 (land) and  $0.42 \pm 0.15$  (ocean) with a Hmax-2km of  $1.29 \pm 0.49$  km (land) and  $1.96 \pm 0.63$  km (ocean). As a  
 consequence, the map of O<sub>3</sub>-2km pseudo-retrievals from IASI-NG+UVNS (Figure 8) is much closer to  
 reality than for IASI+GOME-2. In particular, high ozone values are less underestimated over Holland and  
 the Mediterranean basin (especially off the coast of East Spain and Southern Italy), where low level ozone  
 490 layers are present.

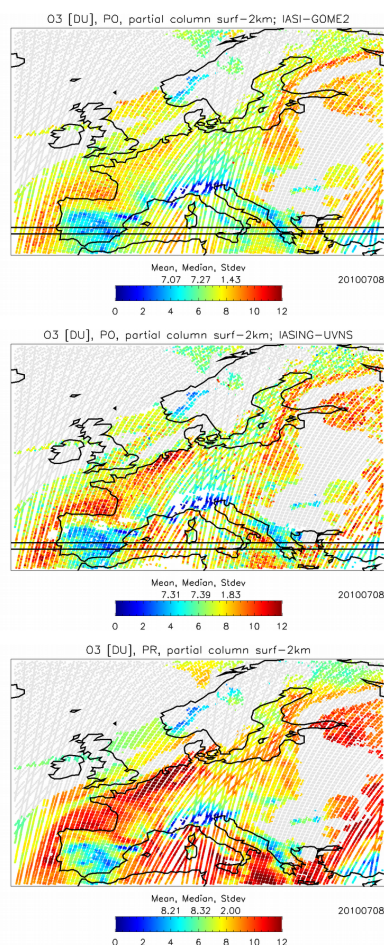


495



Figure 7. IASI+GOME-2 (left) and IASI-NG+UVNS (right) data, for the 08 July 2010. Maps of DOF-2km (top) and Hmax-2km (bottom) pseudo-observations.

500



505 Figure 8. IASI+GOME-2 (top) and IASI-NG+UVNS (middle) pseudo observations of O3-2km and PR  
(bottom) for the 08 July 2010.

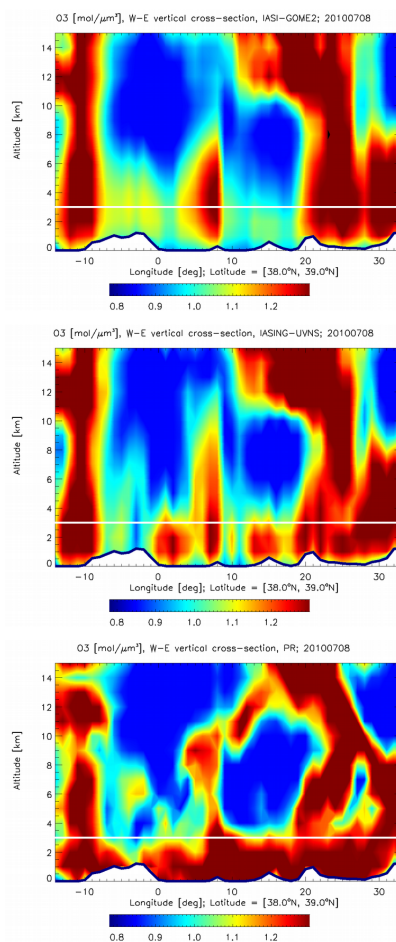
### 6.3 Capacity of resolving layers

510 Along with sensitivity to surface ozone concentrations, vertical resolution of ozone retrievals is the major  
limitations of such products. Indeed, the mixing of vertical information screen out the origin of ozone and  
limits for example their capability to improve models when assimilated.



Figure 9 shows a transect of ozone profiles which allows one to compare the capability of each retrieval to resolve ozone layers. It presents the vertical cross-sections of ozone concentration as observed by IASI+GOME-2 (top) and IASI-NG+UVNS (middle), with the corresponding MOCAGE output (bottom). Data are averaged horizontally with a resolution of 1x1 degrees, along the latitude band [38°N, 39°N]. Both retrieval methods show an overall agreement with pseudo-reality for ozone plumes with concentration higher than 1.0 mol/μm<sup>3</sup>.

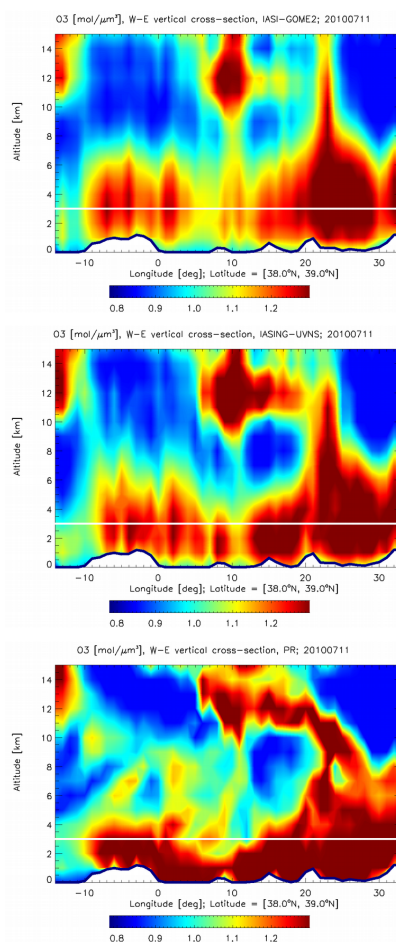
520



525 Figure 9. Cross section of ozone concentration [mol/μm<sup>3</sup>] in the latitude band [38°N, 39°N] (as shown in Figure 5, first row), from the surface to 15 km of altitude, for the 08 July 2010. Data are averaged horizontally with a resolution of 1×1 degrees. (top) IASI+GOME-2 retrievals. (middle) IASI-NG+UVNS retrievals. (bottom) MOCAGE pseudo-reality. White line indicates an altitude of 3 km.



530



535 Figure 10. Same as Figure 9, but for the 11 July 2010.

The comparison of IASI-GOME-2 cross-section with the pseudo-real O<sub>3</sub> concentration confirms that IASI-GOME-2 is able to resolve complex vertical ozone distribution in the lowermost and lower troposphere. This is true for the three ozone peaks (red colour) at [14°W, 10°W], [4°E, 8°E] and [20°E, 30°E] or the moderate O<sub>3</sub> concentrations (yellow-green colour) at [12°W, 5°E] and [9E, 17°E] located below a clean atmosphere. The vertical structures described by IASI+GOME-2 matches well MOCAGE simulations and are consistent with real IASI+GOME-2 product, which is able to observe ozone plumes below 3 km, even if it cannot distinguish whether the ozone plumes are located in the LMT or between 3 and 6km of altitude (Cuesta et al., 2013).

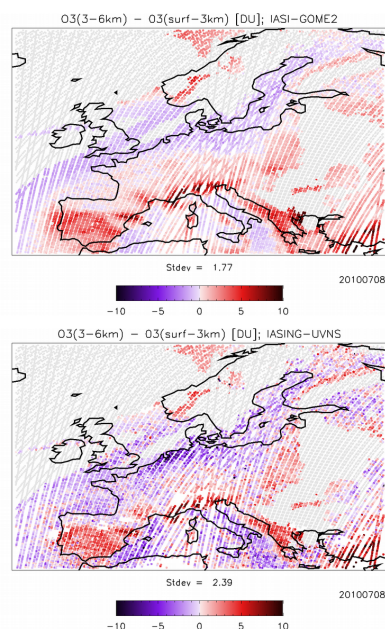
540  
545



IASI-NG+UVNS shows a finer resolution than IASI+GOME-2, resolving ozone layers of 2-3 km thickness below 3 km of altitude. At [0°E, 5°E] and [8°E, 20°E], ozone concentrations higher than 1.2 mol/μm<sup>3</sup> are entirely located in the lowermost troposphere. Even if partially, the scene is captured by IASI-NG+UVNS that is able to depict the signature of LMT ozone, while IASI+GOME-2 fails to detect strong O<sub>3</sub> concentrations.  
550

Same as Figure 9, but for the 11 July 2010, Figure 10 shows the O<sub>3</sub>-3km vertical cross-section in the [38°N, 39°N] latitude band. Again, IASI-NG+UVNS provides more reliable retrievals where ozone concentrations are larger than 1.2 mol/μm<sup>3</sup>, as at [3°E, 10°E] below 4 km (and in particular the peak at [8°E, 10°E] below 2 km) and at [14°E, 19°E] below 3 km. At higher altitudes between 11 and 13 km a.s.l., the 2 km thick ozone layer at [12°E, 20°E] is well resolved by IASI-NG+UVNS but invisible to IASI+GOME-2.  
555

The ability of IASI-NG+UVNS to identify ozone gradient between the 3-6 km and surface-3km analysed in Figure 11, showing maps of pixel-by-pixel difference in ozone partial columns between the two altitude bands. Negative values (in purple) indicate where the O<sub>3</sub> concentration is higher in the LMT. The regional root mean square of the differences is reported in figure, above the colour scale. IASI-NG+UVNS (middle)  
560 clearly shows a better agreement with pseudo-reality (bottom) than IASI+GOME-2 (top), especially over Northern France, Holland and Mediterranean basin.



565

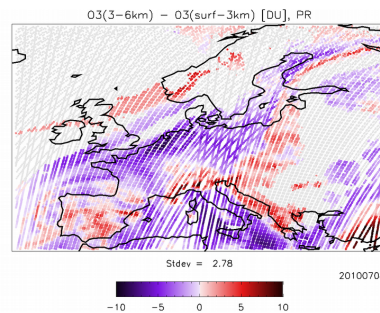


Figure 11. Maps of pixel-by-pixel difference between ozone partial columns [DU] calculated in the surface-3km and 3-6km altitude bands, for the 08 July 2010. Negative values (purple) indicate stronger ozone concentration in the LMT than above. Regional root mean square (RMS) value is reported in figure.  
 570

The same dataset shown in Figure 11 is analysed in Figure 12 as a scatterplot. On the x-axis we present pseudo-reality, on the y-axis the pseudo-observations (black) and the AVK-smoothed pseudo-reality (red).  
 575 Data from IASI+GOME-2 (left, y-axis) and IASI-NG+UVNS (right, y-axis) are compared with pseudo-reality (x-axis). Both methods seem to identify correctly cases where pseudo-real differences are positive, but IASI-NG+UVNS allows to detect negative values (higher ozone concentration in the LMT than above it) down to -8 DU, while IASI+GOME-2 is limited to -2 DU. In case of EPS-SG sensors, the mean error between pseudo-reality and synthetic retrievals is sensibly less biased by -36%.

580

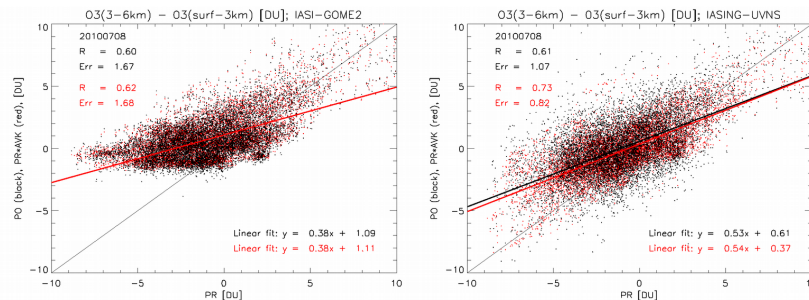


Figure 12. Same data than in Figure 11. (left) IASI+GOME-2 retrievals (black, y-axis), AVK smoothing of pseudo-reality (red, y-axis) and pseudo its pseudo-reality (x-axis). (right) IASI-NG+UVNS retrievals (black, y-axis), AVK smoothing of pseudo-reality (red, y-axis) and pseudo-reality (x-axis). Linear correlation coefficient, mean error and linear fit equation are reported in figure.  
 585

590 **7 Summary and conclusion**

In this work, we quantify the potential of the synergism for LMT ozone retrieval of combining TIR and UV measurements from the new-generation sensors IASI-NG and UVNS (onboard EPS-SG satellite) with respect to the existing IASI+GOME-2 multispectral method. To achieve this goal, we develop a pseudo-observation simulator, where the nature run is defined by output from the MOCAGE model, where real  
595 observation simulator, where the nature run is defined by output from the MOCAGE model, where real ozone data from surface network stations, IASI and MLS instruments have been assimilated for a realistic representation of ozone horizontal variability at the surface and the free troposphere. To ensure the highest degree of reliability with respect to the experiment, the pseudo-real atmosphere has been carefully calibrated by a comparison of real data with the POS of IASI+GOME-2. Cloud fraction, skin temperature and  
600 temperature profile were empirically corrected in order to obtain realistic sensitivity of the satellite products. This calibration stage of meteorological variables important for retrievals appears as a key point of the methodology and we believe it should systematically considered in OSSE. Atmospheric and surface spectra are simulated by KOPRA and VLIDORT radiative transfer codes, performing full and accurate forward and inverse radiative transfer calculations. We analyse and compare pseudo-observations of IASI+GOME-2 and  
605 IASI-NG+UVNS from 8 to 11 July 2010 over Europe. Data assimilation analysis in a different chemical transport model independent from MOCAGE is left to future research work.

Over the whole time period, IASI-NG+UVNS estimates of ozone partial columns, calculated between the surface and 3 km of altitude, are highly correlated to the MOCAGE outputs. With respect to IASI+GOME-2, using new-generation sensors the correlation coefficient between O3-3km pseudo-observations and pseudo-  
610 reality increases on average by about 11%, from 0.65 to 0.73, and the retrieval of high ozone values is less underestimated. As a consequence, the retrieval bias is significantly reduced by -22%. In addition,  $\sigma$ -bias slightly decreases by -5%. The bias between PO and PR gives an estimate of the retrieval method accuracy and is strongly improved mostly because of a higher retrieval sensitivity to true profiles in the lower tropospheric layers (below 2-3km). The  $\sigma$ -bias quantifies the *total error* of the multispectral retrieval and  
615 measures the inversion algorithm precision that remains almost constant when migrating from the existing to the new-generation sensor synergism. This is consistent with the fact that we have designed a specific constrain matrix for IASI-NG+UVNS with the purpose to enhance sensitivity in the lower layers.

With respect to IASI+GOME-2, the main gain of IASI-NG+UVNS relies a on mean DOF-3km increase over both land (from 0.29 to 0.75) and ocean (from 0.21 to 0.66), which is respectively 154% and 208% higher  
620 than using present instrumentation. Accordingly, the mean height of maximum sensitivity in the LMT decreases down to 1.43 km over land and 2.09 km over ocean, which is approximately 1.03 km and 1.30 km below IASI+GOME-2. In addition, IASI-NG+UVNS can also provide reliable ozone retrievals below 2 km of altitude, with an average DOF-2km of 0.52 (land) and 0.42 (ocean) and a mean Hmax-2km of 1.29 km (land) and 1.96 km (ocean). It seems to be able to observe ozone layers of 2-3 km thickness and distinguish  
625 if ozone plumes are located in the lowermost troposphere or just above it, between 3 and 6 km.





This unique capability of IASI-NG+UVNS to provide high confidence O<sub>3</sub> retrievals in the first 2-3 km of the atmosphere should significantly improve regional ozone estimates for air quality studies. Further work should assess the potential impact on ozone forecasts, when assimilating this new multispectral product in a chemical transport model independent from MOCAGE.

630

## References

Amann, M., Bertok, I., Cofala, J., Gyarmas, F., Heyes, C., Klimont, Z., Schoepp, W. and Winiwarter, W. (2005) Baseline Scenarios for the Clean Air for Europe (CAFE) Programme. Final report for the study on  
635 Development of the Baseline and Policy Scenarios and Integrated Assessment Modelling Framework for the Clean Air for Europe (CAFE) Programme-Lot 1 [February 2005]

Barret, B., Le Flochmoen, E., Sauvage, B., Pavelin, E., Matricardi, M., & Cammas, J. P. (2011). The detection of post-monsoon tropospheric ozone variability over south Asia using IASI data. Atmospheric  
640 Chemistry and Physics, 11(18), 9533–9548. <http://doi.org/10.5194/acp-11-9533-2011>

Cai, Z., Y. Liu, X. Liu, K. Chance, C. R. Nowlan, R. Lang, R. Munro, and R. Suleiman (2012), Characterization and correction of Global Ozone Monitoring Experiment 2 ultraviolet measurements and application to ozone profile retrievals, *J. Geophys. Res.*, 117, D07305, doi:10.1029/2011JD017096.  
645

Claeyman, M., Attié, J.-L., Peuch, V.-H., El Amraoui, L., Lahoz, W. A., Josse, B., Joly, M., Barré, J., Ricaud, P., Massart, S., Piacentini, A., von Clarmann, T., Höpfner, M., Orphal, J., Flaud, J.-M., and Edwards, D. P.: A thermal infrared instrument onboard a geostationary platform for CO and O<sub>3</sub> measurements in the lowermost troposphere: Observing System Simulation Experiments (OSSE), *Atmos.*  
650 *Meas. Tech.*, 4, 1637–1661, doi:10.5194/amt-4-1637-2011, 2011a.

Clerbaux, C., Boynard, A., Clarisse, L., George, M., Hadji-Lazaro, J., Herbin, H., Hurtmans, D., Pommier, M., Razavi, A., Turquety, S., Wespes, C., and Coheur, P.-F.: Monitoring of atmospheric composition using the thermal infrared IASI/MetOp sounder, *Atmos. Chem. Phys.*, 9, 6041–6054, doi:10.5194/acp-9-6041-  
655 2009, 2009.

Coman, A., Foret, G., Beekmann, M., Eremenko, M., Dufour, G., Gaubert, B., Ung, A., Schmechtig, C., Flaud, J.-M., and Bergametti, G.: Assimilation of IASI partial tropospheric columns with an Ensemble Kalman Filter over Europe, *Atmos. Chem. Phys.*, 12, 2513–2532, doi:10.5194/acp-12-2513-2012, 2012.  
660

Cuesta, J., Eremenko, M., Liu, X., Dufour, G., Cai, Z., Höpfner, M., von Clarmann, T., Sellitto, P., Foret, G., Gaubert, B., Beekmann, M., Orphal, J., Chance, K., Spurr, R., and Flaud, J.-M.: Satellite observation of



- 665 lowermost tropospheric ozone by multispectral synergism of IASI thermal infrared and GOME-2 ultraviolet measurements over Europe, *Atmos. Chem. Phys.*, 13, 9675–9693, doi:10.5194/acp-13-9675-2013, 2013.
- Dufour, A., Amodei, M., Ancellet, G., and Peuch, V.-H.: Observed and modelled chemical weather during ESCOMPTE, *Atmos. Res.*, 74, 161–189, doi:10.1016/j.atmosres.2004.04.013, 2005.
- 670 Dufour, G., Eremenko, M., Griesfeller, A., Barret, B., LeFlochmoën, E., Clerbaux, C., Hadji-Lazaro, J., Coheur, P.-F., and Hurtmans, D.: Validation of three different scientific ozone products retrieved from IASI spectra using ozonesondes, *Atmos. Meas. Tech.*, 5, 611–630, doi:10.5194/amt-5-611-2012, 2012.
- Dufour, G., Eremenko, M., Orphal, J., and Flaud, J.-M.: IASI observations of seasonal and day-to-day variations of tropospheric ozone over three highly populated areas of China: Beijing, Shanghai, and Hong  
675 Kong, *Atmos. Chem. Phys.*, 10, 3787–3801, doi:10.5194/acp-10-3787-2010, 2010.
- Edwards, D. P., Arellano Jr., A. F., and Deeter, M. N.: A satellite observation system simulation experiment for carbon monoxide in the lowermost troposphere, *J. Geophys. Res.*, 114, D14304, doi:10.1029/2008JD011375, 2009.
- 680 Emili, E., Barret, B., Massart, S., Le Flochmoen, E., Piacentini, a., El Amraoui, L., Cariolle, D. (2014). Combined assimilation of IASI and MLS observations to constrain tropospheric and stratospheric ozone in a global chemical transport model. *Atmospheric Chemistry and Physics*, 14(1), 177–198. <http://doi.org/10.5194/acp-14-177-2014>
- 685 Eremenko, M., Dufour, G., Foret, G., Keim, C., Orphal, J., Beekmann, M., Bergametti, G., and Flaud, J.-M.: Tropospheric ozone distributions over Europe during the heat wave in July 2007 observed from infrared nadir spectra recorded by IASI, *Geophys. Res. Lett.*, 35, L18805, doi:10.1029/2008GL034803, 2008.
- 690 European Organisation for the Exploitation of Meteorological Satellites (EUMETSAT): GOME-2 Level 1 product generation specification, EPS.SYS.SPE.990011, Darmstadt, Germany, 2006.
- Foret, G., Eremenko, M., Cuesta, J., Sellitto, P., Barré, J., Gaubert, B., Coman, A., Dufour, G., Liu, X., Joly, M., Doche, C., and Beekmann, M.: Ozone pollution: What can we see from space? A case study, *J. Geophys. Res. Atmos.*, 119, 8476–8499, doi:10.1002/2013JD021340.
- 695 Fu, D., Worden, J. R., Liu, X., Kulawik, S. S., Bowman, K. W., and Natraj, V.: Characterization of ozone profiles derived from Aura TES and OMI radiances, *Atmos. Chem. Phys.*, 13, 3445–3462, doi:10.5194/acp-13-3445-2013, 2013.



700

Jaumouillé, E., Massart, S., Piacentini, A., Cariolle, D., & Peuch, V.-H. (2012). Impact of a time-dependent background error covariance matrix on air quality analysis. *Geoscientific Model Development*, 5(5), 1075–1090. <http://doi.org/10.5194/gmd-5-1075-2012>

705

Josse, B., Simon, P., and Peuch, V.-H.: Radon global simulations with the multiscale chemistry and transport model MOCAGE, *Tellus B*, 56, 339–356, 2004

710

Koelemeijer, R., Stammes, P., Hovenier, J., and Haan, J. D.: A fast method for retrieval of cloud parameters using oxygen A band measurements from the Global Ozone Monitoring Experiment, *J. Geophys. Res.*, 106, 3475–3490, doi:10.1029/2000JD900657, 2001.

715

Landgraf, J., and O. P. Hasekamp (2007), Retrieval of tropospheric ozone: The synergistic use of thermal infrared emission and ultraviolet reflectivity measurements from space, *J. Geophys. Res.*, 112, D08310, doi:10.1029/2006JD008097.

720

Liu, X., Bhartia, P. K., Chance, K., Spurr, R. J. D., and Kurosu, T. P.: Ozone profile retrievals from the Ozone Monitoring Instrument, *Atmos. Chem. Phys.*, 10, 2521–2537, doi:10.5194/acp-10-2521-2010, 2010.

725

Marécal, V., Peuch, V.-H., Andersson, C., Andersson, S., Arteta, J., Beekmann, M., ... Ung, A. (2015). A regional air quality forecasting system over Europe: the MACC-II daily ensemble production. *Geoscientific Model Development*, 8(9), 2777–2813. <http://doi.org/10.5194/gmd-8-2777-2015>

730

Masutani, M., Woollen, J. S., Lord, S. J., Emmitt, G. D., Kleespies, T. J., Wood, S. A., Greco, S., Sun, H., Terry, J., Kapoor, V., Treadon, R., and Campana, K. A.: Observing system simulation experiments at the National Centers for Environmental Prediction, *J. Geophys. Res.*, 115, D07101, doi:10.1029/2009JD012528, 2010.

735

McPeters, R. D., Labow, G. J., and Logan, J. A.: Ozone climatological profiles for satellite retrieval algorithms, *J. Geophys. Res.*, 112, D05308, doi:10.1029/2005JD006823, 2007.

740

Nowlan, C. R., Liu, X., Chance, K., Cai, Z., Kurosu, T. P., Lee, C., and Martin, R. V.: Retrievals of sulfur dioxide from the Global Ozone Monitoring Experiment 2 (GOME-2) using an optimal estimation approach: Algorithm and initial validation, *J. Geophys. Res.*, 116, D18301, doi:10.1029/2011JD015808, 2011.

745

Rodgers, C. D.: *Inverse methods for atmospheric sounding: Theory and practice*, World Scientific Publishing Company, London, UK, 200 pp., 2000.



Sellitto, P., Dufour, G., Eremenko, M., Cuesta, J., Dauphin, P., Forêt, G., Gaubert, B., Beekmann, M., Peuch, V.-H., and Flaud, J.-M.: Analysis of the potential of one possible instrumental configuration of the next generation of IASI instruments to monitor lower tropospheric ozone, *Atmos. Meas. Tech.*, 6, 621–635, doi:10.5194/amt-6-621-2013, 2013a.

Sellitto, P., Dufour, G., Eremenko, M., Cuesta, J., Peuch, V.-H., Eldering, A., Edwards, D. P., and Flaud, J.-M.: The effect of using limited scene-dependent averaging kernels approximations for the implementation of fast observing system simulation experiments targeted on lower tropospheric ozone, *Atmos. Meas. Tech.*, 6, 1869–1881, doi:10.5194/amt-6-1869-2013, 2013b.

Worden, H. M., Edwards, D. P., Deeter, M. N., Fu, D., Kulawik, S. S., Worden, J. R., and Arellano, A.: Averaging kernel prediction from atmospheric and surface state parameters based on multiple regression for nadir-viewing satellite measurements of carbon monoxide and ozone, *Atmos. Meas. Tech.*, 6, 1633–1646, doi:10.5194/amt-6-1633-2013, 2013.

Worden, J., X. Liu, K. Bowman, K. Chance, R. Beer, A. Eldering, M. Gunson, and H. Worden (2007), Improved tropospheric ozone profile retrievals using OMI and TES radiances, *Geophys. Res. Lett.*, 34, L01809, doi:10.1029/2006GL027806.

Zoogman, P., Jacob, D. J., Chance, K., Zhang, L., Sager, P. L., Fiore, A. M., Eldering, A., Liu, X., Natraj, V., and Kulawik, S. S.: Ozone air quality measurement requirements for a geostationary satellite mission, *Atmos. Environ.*, 45, 7143–7150, doi:10.1016/j.atmosenv.2011.05.058, 2011.

Zyryanov, D., Foret, G., Eremenko, M., Beekmann, M., Cammas, J.-P., D’Isidoro, M., Elbern, H., Flemming, J., Friese, E., Kioutsioutkis, I., Maurizi, A., Melas, D., Meleux, F., Menut, L., Moinat, P., Peuch, V.-H., Poupkou, A., Razinger, M., Schultz, M., Stein, O., Suttie, A. M., Valdebenito, A., Zerefos, C., Dufour, G., Bergametti, G., and Flaud, J.-M.: 3-D evaluation of tropospheric ozone simulations by an ensemble of regional Chemistry Transport Model, *Atmos. Chem. Phys.*, 12, 3219–3240, doi:10.5194/acp-12-3219-2012, 2012.

Zyryanov, D., Foret, G., Eremenko, M., Beekmann, M., Cammas, J.-P., D’Isidoro, M., Elbern, H., Flemming, J., Friese, E., Kioutsioutkis, I., Maurizi, A., Melas, D., Meleux, F., Menut, L., Moinat, P., Peuch, V.-H., Poupkou, A., Razinger, M., Schultz, M., Stein, O., Suttie, A. M., Valdebenito, A., Zerefos, C., Dufour, G., Bergametti, G., and Flaud, J.-M.: 3-D evaluation of tropospheric ozone simulations by an ensemble of regional Chemistry Transport Model, *Atmos. Chem. Phys.*, 12, 3219–3240, doi:10.5194/acp-12-3219-2012, 2012.